

# DynPL-SVO: A New Method Using Point and Line Features for Stereo Visual Odometry in Dynamic Scenes

Baosheng Zhang\*, Ya Wang\*, Xiaoguang Ma, Hong-Jun Ma and Chunbo Luo

**Abstract**—Stereo visual odometry is widely used in which a robot tracks its position and orientation using stereo cameras. Most of the approaches recovered mobile robotics motion based on the matching and tracking of point features along a sequence of stereo images. But in low-textured and dynamic scenes, there are no sufficient robust static point features for motion estimation, causing lots of previous work failed to reconstruct robotic motion. While line features can be detected in low-textured and dynamic scenes.

In this paper, we mainly proposed a new cost function and dynamics grids containing both vertical and horizontal information of features, which can be used in frameworks like `stvo_pl`. The method can work robustly in a wide variety of low-textured and dynamic scenes. Stereo camera motion was obtained through Levenberg-Marquard minimization of re-projection error of point and line features. The experimental results on the KITTI and EuRoC MAV datasets showed that the proposed method had a competitive performance when compared with other state-of-the-art systems by producing more robust and accurate motion estimation in dynamic scenes.

**Index Terms**—Dynamic scenes, motion estimation, line feature, visual odometry (VO).

## I. INTRODUCTION

VISUAL odometry is an emerging and hot research topic in the fields of robotics, autonomous driving and augmented reality. It usually uses a variety of cameras for mobile robotic motion estimation and some works [1] [2] [3] [4] [5] also combined with other kinds of sensors, such as IMU, wheel odometry, and so on. Most systems [6] [7] used points as the only visual feature to get motion estimation since points are

Baosheng Zhang is with the College of Information Science and Engineering, Northeastern University, Shenyang 110819, China (e-mail: zhang-baosheng0503@163.com).

Ya Wang is with the Department of Cognitive Systems, University of Tuebingen, Sand 1, Tuebingen 72076, Germany (e-mail: francis.wang@uni-tuebingen.de).

Xiaoguang Ma is with the State Key Laboratory of Synthetical Automation for Process Industries, Northeastern University, Shenyang 110819, the Foshan Graduate School, Northeastern University, Foshan 528311, China. and College of Information Science and Engineering, Northeastern University, 110819 Shenyang, China (Xiaoguang Ma is the corresponding author, e-mail: maxg@mail.neu.edu.cn).

Hongjun Ma is with the School of Automation Science and Engineering, South China University of Technology, Guangzhou 510641, China, and also with the Key Laboratory of Autonomous Systems and Networked Control, Ministry of Education, Unmanned Aerial Vehicle Systems Engineering Technology Research Center of Guangdong, Guangzhou 510640, China (e-mail: mahongjun@scut.edu.cn).

Chunbo Luo is with the School of Information and School of Information and Communication Engineering, University of Electronic Science and Technology of China, Chengdu 611731, China (e-mail: c.luo@uestc.edu.cn).

\* These authors have contributed equally to this work.

easy to detect, track, and convenient to handle. The popular point feature detectors include oriented FAST and rotated BRIEF(ORB)[8], Scale Invariant Feature Transform(SIFT) [9], and Speeded Up Robust Feature(SURF), etc. Most methods used ORB as a point feature, because of the tradeoff between accuracy and speed. But in low-texture scenes, the systems with only point features can worsen the performance, since it is difficult to find enough reliable point features in an image. In contrast, line segments are usually abundant in any human-made environment, even in low-texture scenes. In addition, the line segment can provide more structural information for motion estimation.

The process of detecting and describing line segments can be handled by Line Segment Detector(LSD) [10] and Line Band Descriptor(LBD) [11], respectively. Line segments with rich structural information can improve the accuracy and robustness of motion estimation. The *Plücker* coordinates of the line had been proposed by Sola [12] to transform and project efficiently, however, over-parameterization of the spatial line will induce gauge freedom and internal consistency constraints [13]. To apply unconstrained optimization, Bartoli [14] proposed the orthonormal representation of lines with a minimum of four parameters, while still having a good performance.

The Jacobian plays an important role in estimating the mobile robotics motion through least-square minimization of the re-projection error between projected and detected features. The Jacobian of the proposed system includes three cost functions, i.e. 1) the distance from projected point features from the previous frame to matched point features in the current frame; 2) the distance between the endpoints of the matched line in the current frame and the projected infinite line from the previous frame; 3) the distance from the midpoints of matched lines to the midpoints of the projected lines. The Jacobians with the above-mentioned cost functions can make the best use of structural information from both point and line features.

A large number of start-of-the-art visual odometry methods are used in real-time and show promising results with high accuracy. However, all these methods [2] [15] [16] can only work well in static scenes. The real-world environment has not only numerous low-texture scenes but also contains a huge number of highly dynamic scenes. Features attached to dynamic objects could reduce the robustness and accuracy of the system. When dealing with dynamic and complex scenes, the traditional method can not get correct inter-frame matching,

resulting in greatly reduced motion estimation accuracy. The idea to solve the above problem is to accurately remove the outliers in images before pose optimization, i.e., the system must remove the features introduced by the dynamic objects and only rely on trusted static features for motion estimation. Therefore, how to accurately extract moving objects and remove the dynamic features is critical to limit the performance of visual odometry (VO) systems.

In this paper, we propose a robust visual odometry system using both point and line features with a novel cost function. Our proposed method mainly solves two issues in the VO/visual simultaneous localization and mapping (vSLAM) systems. On one hand is that in low-texture scenes, traditional *point-only* VO systems can not detect a large set of point features for motion estimation, so more structural information of point and line features is needed to improve its performance in low-texture scenes. In the pose optimization, the spatial line was parametrized by the orthonormal representation. Based on this minimal parametrization, we further derived the analytical Jacobian of the line re-projection error. On the other hand is to solve the issue that dynamic scenes reduce the accuracy of VO using the motion model combines with the dynamic grids to mark dynamic regions and remove dynamic features inside the marked regions before pose optimization.

There are mainly four contributions for the paper.

- We proposed a complete stereo visual odometry system using both point and line features, which can cope with dynamic scenes using only stereo RGB images.
- In pose optimization, we used more structural information of line features. The vertical and horizontal re-projection error of line features and the re-projection error of point features were used to construct a unified cost function, and we further derived the analytical Jacobians of the line re-projection error.
- An effective and fast algorithm was used to remove the outliers using motion model and dynamic grids for visual odometry to solve the problem where dynamic scenes greatly reduced estimation accuracy.
- We conducted extensive comparative experiments on the KITTI dataset for ground vehicles and the EuRoC MAV dataset for aerial vehicles.

## II. RELATED WORK

There are many research fields about visual odometry due to its wide scope of applications, and the visual sensors used mainly include monocular cameras, stereo cameras and RGB-D sensors. Monocular cameras are not as good as stereo systems in initialization and estimation accuracy [1] [17]. The RGB-D camera system can directly obtain the depth information of pixels. However, its application range is limited for outdoor scenes [18] [19]. In the past decades, a lot of researchers [6] [7] paid more attention to stereo visual odometry because of its low cost, robustness and wide range of applications for both indoor and outdoor scenes.

Visual odometry methods can be divided into *direct-based* [20] [21] and *indirect-based (feature-based)* [6] according to visual measurement processing. There are many *feature-based* work, which usually detected a large set of features in

images, such as ORB points. Compared to the *feature-based* methods, the *direct-based* method directly uses intensity for each pixel to compute the camera motion by minimizing photometric errors, instead of detecting and matching features. However, most of the researchers used *feature-based* ones instead due to its robustness and accuracy of estimation.

Most *feature-based* methods detected and tracked point features using a feature descriptor. Then they estimated the motion by minimizing the re-projection errors between the corresponding detected and those projected point features from different frames. To ensure the real-time and reliability of the system, many point *feature-based* researches used the ORB method. These VO systems with only point features can obtain robust and accurate motion estimation in rich-texture scenes. But when facing scenes with poor information or harsh weather, such as a foggy environment, the motion estimation accuracy could degrade significantly. To achieve more robust and better accuracy performance, many researchers introduced line features to improve feature detection capability in the low-texture environment [16] [22] [23].

In order to introduce line features into VO/vSLAM, the first thing we need to do is to detect and match line features in the images. Many researchers achieved good results in line features extraction, such as FLD [24], EDLine [25] and Line Segment Detector(LSD) [10]. Among the above-mentioned methods, LSD is significantly better than other straight-line features detection methods in shortening straight lines and in blurred images. Therefore, we used LSD as a line segment detector from stereo images and Line Band Descriptor(LBD) [11] for line description.

How to represent a line segment in the system has always been a key issue in feature extraction, and the most intuitive and concise way is to use two endpoints to model a 3D line as in [26]. Besides, line features can be represented as infinite lines as in [27], utilizing *Plücker* coordinates to represent the infinite line in VO/vSLAM for more convenient projection and transformation of line features. If the position of the spatial lines is used as the key to the change of the re-projection error, all of the above methods have over-parameterized problems. In order to avoid optimization constraints due to the over-parameterized representation of line features in the optimization process, a lot of work [3] [16] cited the *Plücker* coordinate representation and the orthogonal representation [14] to realize the transformation and optimization, respectively, of the line features. However, we solved the issue by using the Jacobian relationship between the endpoints and the vertical re-projection errors of the line features.

The representation of the line features is different, and the corresponding cost function for optimization is also different. Koletschka [26] took the euclidean distance sum between equally spaced sampling points on the line segment as the cost function of the line features. Since the endpoints of the line detected by LSD are not stable, the line re-projection error was defined as a vector formed by the euclidean distance from the endpoints of the detected line segment in the current frame and the line projected in the previous frame in most methods [3] [16] [23] [27]. All the above cost functions can be easily formed by using the *Plücker* coordinate and the

distance formula between points and lines. However, these methods only paid attention to structural information in the vertical direction of the line features, ignoring rich structural information in the horizontal direction of the line features. Based on the original cost function, the euclidean distance from the projected midpoints of the line segments in the first frame and the midpoints of the lines detected in the second frame was introduced into the new cost function. Our proposed cost function takes advantage of the structural information in both horizontal and vertical directions of the line features.

Estimating motion in dynamic scenes is also one of the open challenges in visual odometry. To deal with this problem, many methods had been proposed. Some work [4] [5] [28] used vision information to fuse other sensors (such as IMU, wheel odometry, and so on) to reduce the impact of dynamic scenes in motion estimation. In addition, there are a large number of methods [29] [30] using RGB-D information to identify dynamic region. The unstable point features in the dynamic region were eliminated to ensure that only stable static point features were retained in the optimization part. Recently, learning-based computer visual methods are emerging, and there are also many feasible solutions [31] [32] to handle the impact of dynamic scenes on visual odometry by combining learning methods. However, the above-mentioned solutions all have strict requirements on scenario conditions and computer resources.

In this paper, we propose a stereo visual odometry method that can achieve high accuracy motion estimation without directly using image depth information and other sensor assistance in dynamic scenes.

### III. DETECTION AND PRE-PROCESSING

In this section, we mainly introduced the front end of the proposed visual odometer system, including the detection and matching in each stereo image of visual features (point and line segment), the definition of *dynamic grid* and the parameterization of line segments.

#### A. Feature detection and matching

1) *Point features*: The performance of features detection work will directly affect the running time and motion estimation accuracy. The focus of point features detection is to ensure the real-time performance of the system, meanwhile detecting as many stable point features as possible. There are large amounts of point features that can be used, like ORB, which is not only fast to compute but also has been verified to be sufficient to meet the need of the system [6]. Therefore, the ORB method was utilized to detect stable point features in the stereo images and describe each detected point feature.

After detecting the point features in left  $p_l(u_l, v_l)$  and right  $p_r(u_r, v_r)$  images of a stereo frame (see Figure 1), it is required to match point features between the left and right images, we meshed all point features of stereo images, i.e. divided the image evenly into  $64 \times 48$  grids and stored all point features according to their grid positions in the image. After that, we used the ORB point feature  $p_l$  in the  $grid(a_p, b_p)$  in the left image to match the point feature  $p_r$  to be matched

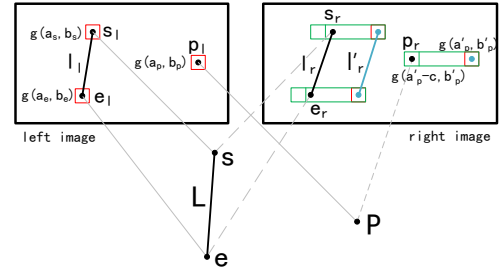


Fig. 1. The feature matching process between the left and right images in the new stereo frame. Considering the epipolar constraint and imaging principle of the stereo camera, we assumed that the point  $p_l$  detected in the left image in the  $grid(a_p, b_p)$  (red square), and the point  $p_r$  to be matched in the range from  $grid(a'_p - c, b'_p)$  to  $grid(a'_p, b'_p)$  in the right image, i.e. the green rectangular area. Same as point matching, the endpoints of the line  $l_r$  detected in the right image meet the matching rule, so it will be the candidate line of  $l_l$ .

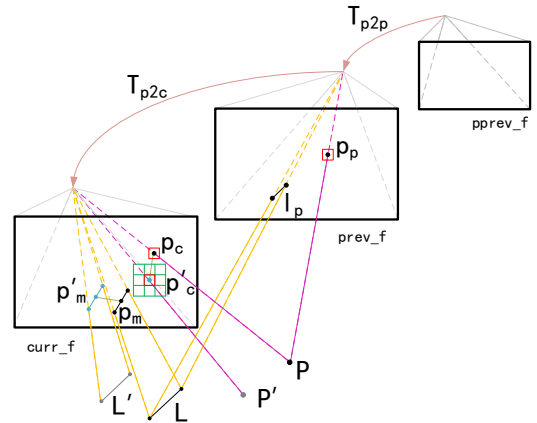


Fig. 2. The features tracking process between adjacent frames.  $T_{p2p}$  denoted the pose transformation between the previous frame  $prev\_f$  and its previous frame  $pprev\_f$ ,  $T_{p2c}$  denoted the pose transformation between the  $prev\_f$  and the current frame  $curr\_f$ . The dynamic spatial point  $P$  and spatial line  $L$  moved to  $P'$  and  $L'$  during sampling time. There was a large error between the dynamic matched point features  $p'_c$  and the point features  $p_c$  estimated by the point features  $p_p$  in  $prev\_f$ , we calculated the error of the surrounding point features and determined *dynamic grid* in green. For line features  $L$ , we used the re-projection error between the midpoints ( $p'_m, p_m$ ) of the matched and estimated line features to find dynamic line features.

in the right image. The feature matching in the stereo camera must follow the epipolar constraint, i.e.  $v_l = v_r$ , and consider the imaging principle of the stereo camera, i.e.  $u_l > u_r$ . The point features to be matched on the right image only include the point features in the horizontal  $c$  grids, ranging from  $grid(a_p - c, b'_p)$  to  $grid(a'_p, b'_p)$  in the right image. This not only greatly improved feature matching efficiently, but also largely avoided the existence of error matching. A mutual consistency check was performed, i.e. the best-left match must correspond to the best-right match, and only these matches were considered valid and used for triangulation.

Figure 2 showed the features tracking process between adjacent frames. In order to avoid the influence of a large number of features attached to dynamic objects on the estimation

results, we used the motion model, i.e., the pose transformation matrix  $T_{p2p}$  between the previous frame  $prev\_f$  and the  $pprev\_f$ , which denotes the previous frame of the  $prev\_f$ , to estimate the location of the matched point features of  $p_c$  in the current frame. Since individual dynamic objects have more abnormal motion relative to the entire stationary scene, i.e. the dynamic spatial point  $P$  moved to  $P'$  during sampling time. The most intuitive response is that the dynamic features  $p'_c$  have a larger re-projection error relative to the features  $p_c$  estimated by the motion model. We calculated and averaged the sum of squared re-projection errors between the matched point features and the estimated point features of the detected point features in all the above grids. Once the value exceeds the threshold, the grid and its surrounding 8 grids in green are determined as *dynamic grid*, and the features in the dynamic grid are dynamic features.

Algorithm 1 shows the detail process of our proposed dynamic region marking based on the determined *dynamic grid* algorithm.

---

**Algorithm 1** : Dynamic region marking using *dynamic grid*

**Input:** Motion model  $T_{p2p}$  of the previous frame  $prev\_f$ , the matched point feature set between the current frame  $curr\_f$  and  $prev\_f$ ;

**Output:** The location of the *dynamic grid*.

```

1: Divide  $curr\_f$  evenly into  $64 \times 48$  grids and only keep
 $n(n \leq 8)$  point features  $p_j$  in each grid  $g_i$ ;
2: for each  $g_i \in curr\_f$  do
3:   for each  $p_j \in g_i$  do
4:      $e_{g_i} += PointErr(p_j, T_{p2p})$ 
5:   end for
6:   if  $e_{g_i} > \rho$  then
7:      $GRIDS\_LOCATION += \{(x_{g_i} - 1, y_{g_i} -$ 
1:    $1), (x_{g_i} + 1, y_{g_i} + 1)\}$ 
8:   end if
9: end for
10: return  $GRIDS\_LOCATION$ 

```

---

2) *Line features*: The detection of line features faces more challenges. In real-world scenes, some factors, such as changes of lighting, different point of views, and occlusions make it hard for all detected line features to be stable. The focus of line feature detection is to reduce running time and to improve robustness to light. LSD is a popular line segment detector, widely used in computer vision. It is designed to work on noisy images in various scenes without parameter tuning, and the detected line meets the system requirements in terms of accuracy.

Since the endpoints of the line detected by LSD are not stable, the line cannot be perfectly matched only using its endpoints. Similar to point features matching between the left and right images, we meshed the line features in the right image, i.e. all line features passing through the same grid in the image on the right were managed uniformly. We assumed the grids, where the two endpoints of the line feature  $l_l$  in the left image were located  $(a_s, b_s)$  and  $(a_e, b_e)$ , then we selected the line features to be matched within the corresponding grid range in the right image, and only the line  $l_r$  meet the line matching

rule will be selected as the candidate line of  $l_l$ , as depicted in Figure 1. A mutual consistency check was again performed, i.e. the best-left match must correspond to the best right match, and only these matches that meet the above requirements can participate in the follow-up work.

As shown in Figure 2, for the dynamic line features tracking process between adjacent frames, we used the re-projection error between the estimated line midpoint  $p_m$  and the matched line midpoint  $p'_m$  as the judgment basis. Once the value exceeded the preset threshold, we determined that the line feature was a dynamic line feature and removed it.

### B. Representation of Line Features

A 3D point can be represented by Euclidean spatial coordinates. However, the representation of line features in space is a challenging task. We assumed the homogeneous coordinates of line endpoints are  $\bar{X}_s(x_1, y_1, z_1, w_1)$  and  $\bar{X}_e(x_2, y_2, z_2, w_2)$ , respectively, while their inhomogeneous coordinates were represented as  $X_s, X_e$ . Then the *Plücker* coordinates of the line  $L$  can be constructed as follows:

$$L = \begin{bmatrix} X_s \times X_e \\ w_2 X_s - w_1 X_e \end{bmatrix} = \begin{bmatrix} \mathbf{n} \\ \mathbf{d} \end{bmatrix} \in \mathbb{R}^6 \quad (1)$$

, where  $\mathbf{n}$  and  $\mathbf{d}$  are 3-dimensional vectors,  $\mathbf{d}$  is the direction vector of the line and  $\mathbf{n}$  is the normal vector of the plane determined by the line and the origin, i.e.  $\mathbf{n}^T \times \mathbf{d} = 0$ . The *Plücker* coordinates  $L$  can also be extracted from the dual *Plücker* matrix  $T^*$ . The dual plucker matrix can be defined as follows:

$$T^* = \begin{bmatrix} \mathbf{d}^\wedge & \mathbf{n} \\ -\mathbf{n}^T & 0 \end{bmatrix} \quad (2)$$

The representation of *Plücker* coordinates is convenient for both line feature projection and transformation.

In a nutshell, in the proposed visual odometry system, we used the motion model to find the dynamic features, and we used *Plücker* coordinates to parameterize the line features. In addition, a simple and effective Jacobian matrix perfectly solved the over-parameterized problem of the *Plücker* coordinates.

## IV. MOTION ESTIMATION

In this section, we presented in detail how the point and line measurements were introduced in our system and motion estimation were performed. In addition, we derived the analytical Jacobians of re-projection error with respect to point and line feature parameters.

### A. Problem Statement

We had obtained the point and line features in a sequence of images and their plural positions in camera frames. The problem to be solved is how to find the optimal transformation that satisfies projection constraints of the corresponding features as much as possible. This can be solved by a non-linear least-square equation formed by the projection constraints of

the corresponding features in the previous frame and current frame.

Different from other point-line VO/vSLAM systems with the re-projection error of point features and vertical re-projection error of line features, the proposed method not only retained the above two kinds of re-projection error but also introduced the horizontal re-projection error of line features into the motion estimation. This can make full use of the structural characteristics of the line features and improve system robustness and accuracy. So the non-linear least-square equation of our approach as shown in (3).

$$\xi^* = \arg \min_{\xi} \left[ \sum_{i=1}^m e_p^i(\xi)^T \Sigma_{e_p^i}^{-1} e_p^i(\xi) + \sum_{j=1}^n e_{l_v}^j(\xi)^T \Sigma_{e_{l_v}^j}^{-1} e_{l_v}^j(\xi) + \sum_{k=1}^q e_{l_h}^k(\xi)^T \Sigma_{e_{l_h}^k}^{-1} e_{l_h}^k(\xi) \right] \quad (3)$$

, where  $m, n$  and  $q$  denote the number of points, all lines and the lines complete in image, respectively. It consisted of the point re-projection error  $e_p^i$ , vertical and horizontal re-projection error of line feature  $e_{l_v}^j, e_{l_h}^k$ . The matrices  $\Sigma^{-1}$  in (3) represent the inverse covariance matrices related to the uncertainty of each re-projection error.

The re-projection error of points were defined as the distance between the projected point features from the previous frame to the detected point features in the current frame:

$$e_i^p = p_i - p'_i(\xi) \quad (4)$$

, where  $p_i, p'_i(\xi)$  represent point detected from current frame and point projected from the previous frame into current frame, respectively.

Compared with point features, it is a challenging task to introduce the re-projection error of line features in optimization. In most methods, only the vertical re-projection errors of the line features were introduced into the motion estimation, i.e. the distance from the endpoints of the detected line features to the projected infinite line features, shown as

$$e_j^{l_v} = \begin{bmatrix} d(l_j, p'_{j,s}(\xi)) \\ d(l_j, p_{j,e}(\xi)) \end{bmatrix} \quad (5)$$

, where  $p'_s$  and  $p'_e$  denote the endpoints of the line features and  $d(\cdot)$  represent the distance function from point to line.

In our method, the horizontal re-projection error of the line features was introduced into the optimization part by using the re-projection error of the midpoints of the line features:

$$e_k^{l_h} = p_{i,m} - p'_{i,m}(\xi) \quad (6)$$

, where  $p_{i,m}, p'_{i,m}(\xi)$  represent midpoint of the line detected from current frame and projected from previous frame, respectively.

The pose optimization problem in (3) can be iteratively solved using the Gauss-Newton and Levenberg-Marquardt algorithm. To do this, we need to derive the Jacobian of the point and line feature re-projection errors. In the next section, we will illustrate the Jacobian of the three above-mentioned re-projection errors of point and line features.

## B. Jacobian Matrix of Point and Line Re-Projection Errors

In order to derive the Jacobian of feature re-projection error, we converted the pose transformation to Lie algebra form, i.e. using six-dimensional vectors  $\xi \in \mathfrak{se}(3)$  to represent the pose transformation matrix  $T \in SE(3)$ . So the Jacobian of a point features can be expressed as:

$$J_p = \frac{\partial e_i^p}{\partial \delta \xi} = \frac{\partial e_i^p}{\partial P'} \frac{\partial P'}{\partial \delta \xi} \quad (7)$$

, where  $P'$  represent 3D point of matched point feature from previous frame in current camera frame. The above Jacobian can be divided into two parts by the chain rule. The first part can be expressed by the camera projection principle as the following equation:

$$\frac{\partial e_i^p}{\partial P'} = - \begin{bmatrix} \frac{\partial u}{\partial X'} & \frac{\partial u}{\partial Y'} & \frac{\partial u}{\partial Z'} \\ \frac{\partial v}{\partial X'} & \frac{\partial v}{\partial Y'} & \frac{\partial v}{\partial Z'} \end{bmatrix} = - \begin{bmatrix} \frac{f_x}{Z'} & 0 & -\frac{f_x X'}{Z'^2} \\ 0 & \frac{f_y}{Z'} & -\frac{f_y Y'}{Z'^2} \end{bmatrix} \quad (8)$$

For the second part, we can obtain the following results through the Lie algebra perturbation model:

$$\frac{\partial P'}{\partial \delta \xi} = \frac{\partial TP}{\partial \delta \xi} \Rightarrow [I \quad -P'^{\wedge}] \quad (9)$$

, where  $[\cdot]^{\wedge}$  denotes the skew-symmetric matrix of a vector. So, the Jacobian of point re-projection error can be constructed as (10).

$$J_p = \frac{\partial e_i^p}{\partial \delta \xi} = \frac{\partial e_i^p}{\partial P'} \frac{\partial P'}{\partial \delta \xi} = - \begin{bmatrix} \frac{f_x}{Z'} & 0 & -\frac{f_x X'}{Z'^2} & -\frac{f_x X' Y'}{Z'^2} & f_x + \frac{f_x X'^2}{Z'^2} & -\frac{f_x Y'}{Z'} \\ 0 & \frac{f_y}{Z'} & -\frac{f_y Y'}{Z'^2} & -f_y - \frac{f_y Y'^2}{Z'^2} & \frac{f_y X' Y'}{Z'^2} & \frac{f_y X'}{Z'} \end{bmatrix} \quad (10)$$

More detailed information can be found in [3] [16].

We divided the re-projection error of line features  $e_l$  into horizontal  $e_{lh}$  and vertical  $e_{lv}$ , i.e.  $e_l = e_{lh} + e_{lv}$ . Vertical re-projection error is similar to the expression in [15] [27], and can be defined as (5). Firstly, we converted the 3D line  $L_w$  from the world frame to the current camera frame as follows:

$$L_c = \begin{bmatrix} \mathbf{n}_c \\ \mathbf{d}_c \end{bmatrix} = T_{cw} L_w = \begin{bmatrix} R_{cw} & (t_{cw})^{\wedge} R_{cw} \\ 0 & R_{cw} \end{bmatrix} L_w \quad (11)$$

, where the  $R_{cw}$  and  $t_{cw}$  represent the rotation matrix and translation vector from the world frame to the camera frame, respectively.

Then, the 3D line was projected into the image and described as  $l'$ , according to the known intrinsic parameter matrix of the camera, the projection of 3D line  $L_c$  from the camera frame to normalize image plane can be shown as follows:

$$l' = \mathcal{K} L_c = \begin{bmatrix} f_y & 0 & 0 \\ 0 & f_x & 0 \\ -f_y c_x & -f_x c_y & f_x f_y \end{bmatrix} \mathbf{n}_c = \begin{bmatrix} l_1 \\ l_2 \\ l_3 \end{bmatrix} \quad (12)$$

, where  $\mathcal{K}$  represents the projection matrix of the line. Note that the coordinates of the segment projected by the 3D line is only related to the normal vector  $\mathbf{n}_c$ . Since we projected the line features into the image as an infinite line, so only normal

components  $\mathbf{n}_c$  in the *Plücker* coordinates  $L_c$  can provide meaningful information in the projection.

The vertical re-projection error of the line features can be expressed as follows, as mentioned in Section IV-A.

$$e_j^v = \begin{bmatrix} d_s \\ d_e \end{bmatrix} = \begin{bmatrix} \frac{p_s^T l'}{\sqrt{l_1^2 + l_2^2}} \\ \frac{p_e^T l'}{\sqrt{l_1^2 + l_2^2}} \end{bmatrix} \quad (13)$$

We assumed  $l = \sqrt{l_1^2 + l_2^2}$  and  $d = \frac{\mathbf{p}^T l'}{l}$ . So the Jacobian of vertical re-projection error of line feature can be expressed as:

$$\begin{aligned} \frac{\partial d}{\partial \delta \xi} &= \frac{\partial \mathbf{p}^T l'}{\partial \delta \xi} \\ &= \frac{\partial (u l_1 + v l_2 + l_3)}{\partial \delta \xi} \frac{1}{l} \\ &= [l_1 \quad l_2] \frac{\partial \begin{bmatrix} u \\ v \end{bmatrix}}{\partial \delta \xi} \frac{1}{l} \end{aligned} \quad (14)$$

The following equation can be found using the chain rule:

$$\frac{\partial \begin{bmatrix} u \\ v \end{bmatrix}}{\partial \delta \xi} = \frac{\partial \begin{bmatrix} u \\ v \end{bmatrix}}{\partial P'} \frac{\partial P'}{\partial \delta \xi} \quad (15)$$

Finally, the Jacobian of the vertical re-projection error of the line features can be found by referring to the (10) as follows:

$$\begin{aligned} \frac{\partial d}{\partial \delta \xi} &= - [l_1 \quad l_2] \\ &\begin{bmatrix} \frac{f_x}{Z'} & 0 & -\frac{f_x X'}{Z'^2} & -\frac{f_x X' Y'}{Z'^2} & f_x + \frac{f_x X'^2}{Z'^2} & -\frac{f_x Y'}{Z'} \\ 0 & \frac{f_y}{Z'} & -\frac{f_y Y'}{Z'^2} & -f_y - \frac{f_y Y'^2}{Z'^2} & \frac{f_y X' Y'}{Z'^2} & \frac{f_y X'}{Z'} \end{bmatrix} \frac{1}{l} \end{aligned} \quad (16)$$

$$J_{l_v} = d_s \frac{\partial d_s}{\partial \delta \xi} + d_e \frac{\partial d_e}{\partial \delta \xi} \quad (17)$$

Compared to the methods of directly deriving the Lie algebra of the transformation in [3] [16], obtaining the Jacobian of vertical re-projection of the line features is more efficient and convenient using the derivation result of the endpoints of the line.

The Jacobian derivation of the horizontal re-projection errors of the line feature was similar to the expression above. We defined the re-projection error of the matched and projected line midpoints as the cost function of line horizontal re-projection error. The result was shown as the following:

$$\frac{\partial e_k^{l_h}}{\partial \delta \xi} = \frac{\partial e_k^{l_h}}{\partial P'_m} \frac{\partial P'_m}{\partial \delta \xi} \quad (18)$$

, where  $P'_m$  represent 3D midpoint of matched line feature from previous frame to current camera frame.

Referring to (10), we can obtain the Jacobian of line feature horizontal re-projection error as follows:

$$\begin{aligned} J_{l_h} &= \frac{\partial e_k^{l_h}}{\partial \delta \xi} \\ &= - \begin{bmatrix} \frac{f_x}{Z'_m} & 0 & -\frac{f_x X'_m}{Z_m'^2} & -\frac{f_x X'_m Y'_m}{Z_m'^2} & f_x + \frac{f_x X_m'^2}{Z_m'^2} & -\frac{f_x Y'_m}{Z'_m} \\ 0 & \frac{f_y}{Z'_m} & -\frac{f_y Y'_m}{Z_m'^2} & -f_y - \frac{f_y Y_m'^2}{Z_m'^2} & \frac{f_y X'_m Y'_m}{Z_m'^2} & \frac{f_y X'_m}{Z'_m} \end{bmatrix} \end{aligned} \quad (19)$$

So far, the Jacobians of all feature re-projection errors had been obtained, and we can obtain the pose transformation between adjacent frames by solving the non-linear least-square equation by Levenberg-Marquard algorithm.

## V. EXPERIMENTAL RESULTS AND ANALYSIS

In this section, we evaluated the proposed method on the public KITTI dataset [33] and EuRoC MAV dataset [34]. To verify the performance of our method, we compared the accuracy of our algorithm with the state-of-the-art VO systems that can run with stereo RGB data. The selected methods were stvo\_pl [27], ORB\_SLAM2 [6] and BoPLW [35]. In order to fairly compare all methods, we only kept the front end of ORB\_SLAM2 and BoPLW to form VO systems. In addition, to illustrate the benefits of the line feature horizontal re-projection error on the accuracy of motion estimation, we showed the results of our proposal with only horizontal or vertical re-projection errors. Finally, we evaluated the ability of dynamic grids to cope with dynamic scenes on highly dynamic sequences. For that, we estimated the trajectory of a stereo camera in several video sequences with moving objects.

All the experiments had been run on an Intel Core i5-4210U CPU @ 1.70GHz  $\times$  4 and 16 GB RAM without GPU. In the evaluation of the system's ability to deal with dynamic environmental issues, since there are no dynamic objects in the EuRoC MAV dataset, the effect of the dynamic grid method is limited, and the dynamic grids to improve the system to cope with dynamic environments cannot be well demonstrated. So, we only estimated the trajectory of our method with or without dynamic grids in the KITTI dataset.

### A. KITTI

We had tested the proposed method on the well-known KITTI dataset, which provided ground truth trajectories based on a 64 channels Velodyne LiDAR sensor and a GPS localization system. The stereo images were captured by two grayscale cameras (FL2-14S3M-C) attached to the top of a car. Since this dataset has highly textured urban scenes with light changes, it is closer to the real autonomous driving scenes, and the dynamic scenes containing moving objects like cars and pedestrians in some image sequences have a great impact on the performance of the VO/vSLAM systems. To verify that the proposed method has an outstanding performance on accuracy, we showed both absolute pose error in table I and relative pose error in table II, compared to three other systems, i.e. stvo\_pl, ORB\_SLAM2 front end, and BoPLW front end. On one hand, in table I with absolute pose error comparisons, we listed the root-mean-square error (RMSE) of absolute translation errors

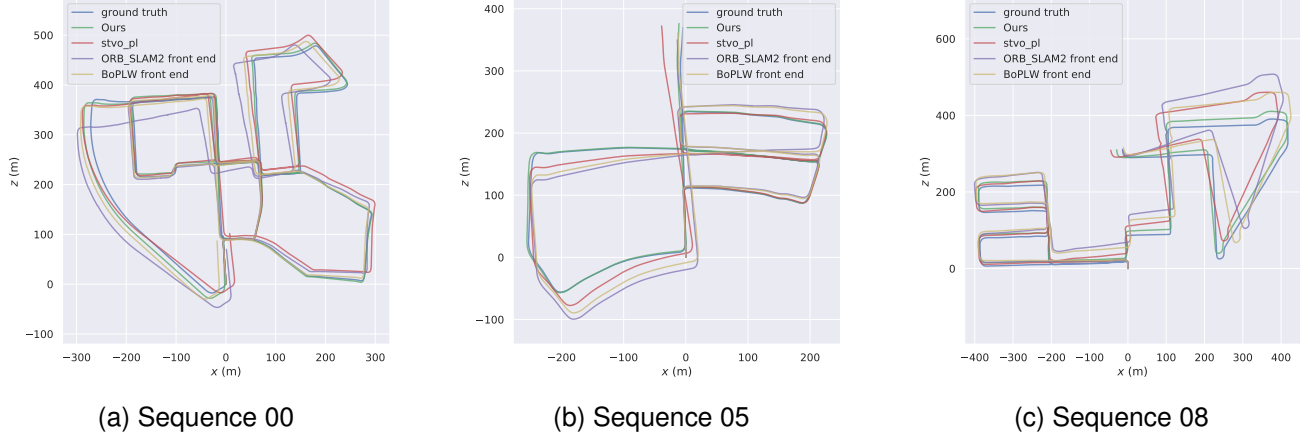


Fig. 3. Reconstruction of the path from our algorithm, stvo\_pl and ORB\_SLAM2 front end. The ground truth is represented with blue lines, the green lines represent the estimation of our method, the red lines represent the estimation of stvo\_pl, the path provided by ORB\_SLAM2 and BoPLW are plotted with purple and brown lines, respectively. (a) Top view of the Sequence 00 path. (b) Top view of the Sequence 05 path. (c) Top view of the Sequence 08 path.

TABLE I  
ABSOLUTE RMSE IN THE KITTI DATASET, NOTE THAT THE DASH INDICATES THAT THE EXPERIMENT FAILED.

Seq.	Ours		stvo_pl		ORB_SLAM2 front end		BoPLW front end	
	$t_m$	$R_{deg}$	$t_m$	$R_{deg}$	$t_m$	$R_{deg}$	$t_m$	$R_{deg}$
00	<b>6.691</b>	1.788	7.426	2.105	14.076	3.461	7.551	<b>1.519</b>
01	<b>172.502</b>	<b>8.910</b>	371.245	12.212	-	-	-	-
02	21.653	4.423	<b>8.167</b>	<b>1.505</b>	14.187	2.615	11.276	2.550
03	6.077	4.308	6.030	3.310	<b>2.317</b>	1.511	3.018	<b>1.466</b>
04	<b>2.100</b>	<b>29.944</b>	2.216	34.067	2.655	49.025	2.550	38.861
05	<b>4.097</b>	<b>1.598</b>	6.506	2.695	11.755	4.217	8.750	3.641
06	<b>4.113</b>	2.927	5.564	6.305	4.219	<b>1.518</b>	4.120	2.364
07	5.216	<b>1.957</b>	<b>3.028</b>	2.165	14.155	5.698	15.512	6.957
08	<b>7.202</b>	<b>3.019</b>	10.054	3.254	24.796	6.134	17.134	3.302
09	<b>4.729</b>	<b>1.065</b>	12.205	2.454	18.387	3.718	24.154	4.288
10	<b>2.064</b>	1.831	2.649	<b>1.155</b>	3.823	2.081	4.992	1.823

and rotation errors for the proposed method and the compared approaches, where our method had a better performance than other methods in 9 sequences and the proposed approach enhances 24.8% accuracy compared to traditional approaches in same experimental sequence. The result showed that our method presented better accuracy performance in terms of motion estimation in most sequences, especially in the dynamic ones. On the other hand, in table II with relative pose errors comparisons, the result showed that our system achieves more accuracy than other comparative experimental systems in most scenes. Figure 3 showed the reconstruction of the path from our algorithm, stvo\_pl, ORB\_SLAM2 front end and BoPLW front end on several sequences of the KITTI dataset that present dynamic objects and a lot of challenging scenes. It is observed that the reconstructed paths from compared systems had larger deviation than the proposed approach in all experimental sequences, especially around corners with large point of view changes. This means that the proposed method obtained more accurate absolute solutions than other experimental systems in dealing with challenging and dynamic environments. The reason is the introduce dynamic grids and horizontal re-projection error into the proposed method.

We compared our approach with BoPLW on the KITTI dataset, the BoPLW is a visual SLAM approach to expand

from ORB\_SLAM2 with line features. as shown in table I, our method had higher accuracy result values than BoPLW in most sequences. As an illustrative example, Figure 4 showed the distribution of the features during motion estimation on KITTI-01. There are large numbers of dynamic objects, such as moving cars, in the dataset scene. Our method outperforms other methods in the dynamic environment. One of the reasons is the use of dynamic grids to remove the dynamic point features, but in other methods, a lot of features on dynamic objects were used to estimate the motion of the camera, which results in error estimation. Eventually, the task execution failed due to the insufficient number of stable features, such as the ORB\_SLAM2 and BoWPL front end shown in table I and table II. The line feature introduction ensures that our system and stvo\_pl run stably in all scenes, and the additional horizontal errors of the line features make our system achieve more accurate results than stvo\_pl.

Finally, we also did an ablation study on different directions of line features in our system, yielding the results presented in table III. We can observe that the system with only the horizontal error has a more accurate result than only with the vertical error in almost all sequences of the KITTI dataset, especially on relative errors. The horizontal re-projection error achieves more accuracy in 10 sequences than the system with-

TABLE II  
MEAN RELATIVE POSE ERRORS ON THE KITTI DATASET, NOTE THAT THE DASH INDICATES THAT THE EXPERIMENT FAILED.

Seq.	Ours		stvo_pl		ORB_SLAM2 front end		BoPLW front end	
	t%	R <sub>deg/100m</sub>	t%	R <sub>deg/100m</sub>	t%	R <sub>deg/100m</sub>	t%	R <sub>deg/100m</sub>
00	1.569	0.443	1.607	0.405	1.424	0.590	<b>1.137</b>	<b>0.366</b>
01	<b>21.339</b>	<b>1.402</b>	43.723	1.939	-	-	-	-
02	1.733	0.517	1.738	<b>0.344</b>	1.621	0.508	<b>1.581</b>	0.433
03	3.604	1.637	3.467	1.260	<b>1.964</b>	0.712	2.140	<b>0.639</b>
04	<b>1.907</b>	0.424	2.023	<b>0.282</b>	2.447	0.498	3.398	0.511
05	<b>1.007</b>	<b>0.375</b>	1.412	0.493	2.649	0.754	2.405	0.609
06	1.898	0.582	2.372	<b>0.506</b>	1.974	0.524	<b>1.761</b>	0.567
07	2.051	<b>0.879</b>	<b>1.725</b>	1.047	4.658	2.138	5.067	2.542
08	<b>1.279</b>	<b>0.453</b>	1.670	0.468	3.121	0.959	2.642	0.608
09	<b>1.486</b>	<b>0.353</b>	2.129	0.465	3.422	1.044	4.388	0.933
10	1.204	0.572	<b>1.032</b>	<b>0.337</b>	1.693	0.716	1.903	0.566



Fig. 4. Picture from *KITTI-01*. The green points represent point features and green lines represent line features. There are many features attached to the moving cars which will reduce the robustness of the result, even failed.

TABLE III  
MEAN ABSOLUTE AND RELATIVE RMSE ERRORS ON THE KITTI DATASET.

Seq.	wo/line error		w/vertical error		w/horizontal error	
	APE	RPE	APE	RPE	APE	RPE
00	7.3728	0.0323	11.9514	0.0391	<b>6.6818</b>	<b>0.0322</b>
01	<b>52.5071</b>	<b>0.7188</b>	166.6740	1.0059	89.8455	0.7788
02	20.6018	0.0348	23.6016	0.0559	<b>19.5024</b>	<b>0.0346</b>
03	6.2301	<b>0.0317</b>	<b>6.0842</b>	0.0322	6.2207	<b>0.0317</b>
04	2.7768	0.0374	<b>2.2843</b>	0.0554	2.7410	<b>0.0365</b>
05	3.9010	0.0182	4.3099	0.0196	<b>3.8735</b>	<b>0.0181</b>
06	5.0703	0.0326	<b>4.6390</b>	0.0448	4.9705	<b>0.0322</b>
07	<b>1.5365</b>	0.0178	5.4844	0.0634	1.8679	<b>0.0174</b>
08	5.4780	0.0390	7.3161	0.0441	<b>4.8398</b>	<b>0.0389</b>
09	4.5855	0.0248	<b>4.4380</b>	0.0674	4.5637	<b>0.0245</b>
10	2.0184	0.0198	2.2578	0.0342	<b>2.0173</b>	<b>0.0197</b>

out line error and improves average 49.1% accuracy compared to the vertical re-projection error in the KITTI dataset. Figure 5 depicted the matching results of line features between adjacent frames in the sequence KITTI-03. It can be noted that there are still enough stable line features in challenging scenes. The numerous short lines show more superior characteristics in horizontal re-projection errors than vertical. Therefore, the system with horizontal re-projection errors can have a better performance in most sequences, especially in relative errors.

### B. EuRoC MAV

The EuRoC MAV dataset, which was collected by a micro aerial vehicle (MAV), including 11 sequences in two indoor scenes. The dataset contains stereo images from a global shutter camera (Aptina MT9V034 global shutter, WVGA monochrome, and 20 FPS) and synchronized inertial measurement unit (IMU, ADIS16448, 200 Hz) [2]. Note that the dataset is an indoor dataset with large rotation movements

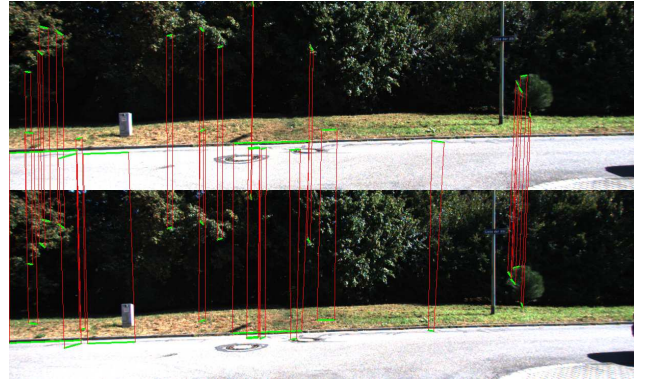


Fig. 5. The matching results of line features between adjacent frames in challenging scenes on *KITTI-03*. The line features are represented with green lines and the match lines are represented with red lines. There are still enough stable line features in challenging scenes for horizontal re-projection errors to improve pose estimation.

of drones, and there are a lot of line features in the indoor environment for motion estimation. We ran our method and *stvo\_pl* for comparison. In addition, to verify that the horizontal re-projection errors of the line features have an optimized effect on estimation accuracy, we also ran the method only with horizontal and vertical re-projection errors, respectively, on the EuRoC MAV dataset.

As an example, Figure 6(a) showed the line features extraction in the *V2\_01\_easy* sequence, Figure 6(b) and 6(c) respectively showed the line features before and after the optimization process in the motion estimation. There are a large amount of short but complete lines in the scene, as mentioned above, horizontal re-projection errors show more superior characteristics in this case than vertical re-projection errors. At the same time, we observed good performance of all line features pose optimization by minimizing re-projection errors. Table IV shows that the systems with horizontal re-projection error, i.e. our system and the system with only horizontal error, provided more accurate results in 9 experimental scenes of the EuRoC MAV dataset, even in the indoor and static environment, the ablation study shows that the horizontal error plays a more important role than the vertical error in most sequences, and our proposed method also had higher accuracy than *stvo\_pl*, such as *MH\_01\_easy*, *MH\_04\_different* etc. The reasons are that there are many short but complete lines in

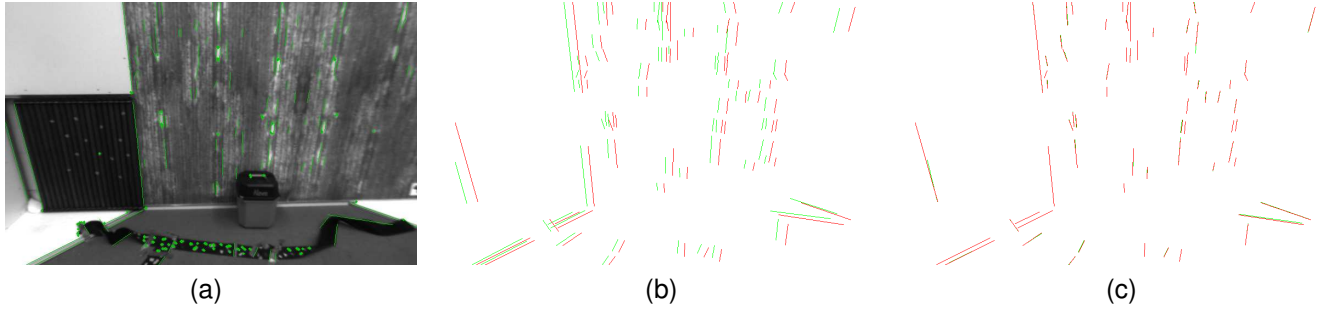


Fig. 6. The tracking of line features in the process of motion estimation. (a) The result of features detection on V2\_01\_easy. (b) Showed the line features before pose optimization, the green lines represent detected line segments from the current frame, and the red lines represent re-projected line segments from the previous frame. (c) Showed the result of motion estimation. There are also numerous stable short line features in indoor scenes, which can be efficient for optimization by horizontal re-projection errors.

TABLE IV  
MEAN RELATIVE RMSE ON THE EUROC MAV DATASET.

Sequence	stvo_pl	Ours	ours w/vertical error	ours w/horizontal error
MH_01_easy	0.033349	<b>0.033276</b>	0.033294	0.033358
MH_02_easy	0.032896	0.032547	0.032501	<b>0.032016</b>
MH_03_med	0.073692	0.072181	0.071908	<b>0.071196</b>
MH_04_dif	0.103936	<b>0.103109</b>	0.103346	0.103473
MH_05_dif	0.095603	<b>0.094194</b>	0.094640	0.094608
V1_01_easy	<b>0.048642</b>	0.049194	0.049011	0.049427
V1_02_med	0.102017	0.102235	0.102260	<b>0.101900</b>
V1_03_dif	0.098576	0.101252	0.101670	<b>0.097804</b>
V2_01_easy	0.037155	<b>0.032626</b>	0.032655	0.032629
V2_02_med	0.074001	0.071558	0.073592	<b>0.071348</b>

the sequences and the use of horizontal re-projection errors in our method helps improve the performance. This experiment proved that the horizontal re-projection errors have a good performance in motion estimation, even better than the vertical re-projection errors. Besides, our proposed approach can also provide a good result in a static environment.

### C. Evaluation of the ability of dynamic grids to cope with dynamic scenes.

By combining the dynamic grid method with the VO system, the ability of the system to deal with dynamic scenes can be improved. To further verify the effect of dynamic grids on dynamic scenes during motion estimation, a comparative analysis was done to determine the improvement of dynamic grids in a series of dynamic sequences. There are moving objects like cars and people in the KITTI dataset. As Figure 7(a) and Figure 7(b) shown, regardless of whether the scene contains rich structural information, the dynamic grids can identify vehicles traveling at high speeds in different directions. In addition, for dynamic objects that move slowly, such as pedestrians, the dynamic grids can still eliminate dynamic features through the complete market area (see Figure 7(c) and (d)). It verified that the dynamic grids can accurately identify the dynamic regions to avoid the influence of dynamic features on the accuracy, and our proposed method was robust in dynamic scenes. To represent the error in the quantitative analysis, we compared the absolute and relative root-mean-square error (RMSE) with and without dynamic grid approaches in the KITTI dataset. And the result showed in Table V, for each of the tested datasets. It can be noticed

that the system with the dynamic grid method has a more accurate estimation in 8 sequences and enhances about 15% accuracy compared to the traditional approaches. Especially, the dynamic grid method worked well in sequences (such as KITTI-01,05,09) with highly dynamic scenes, even improved accuracy more than 30%. However, when there are large numbers of unstable scenes in the surrounding environment, such as the KITTI-02 with the presence of a large number of non-artificial environments and the lack of dynamic objects, the accuracy of the results was estimated by our method degrades. The main reason is that the dynamic grids mark some unstable positions like leaves as dynamic regions, which reduce the number of features involved in motion estimation and decrease the accuracy of the results. The results proved that our method gave much stable and higher accuracy motion estimation in a dynamic environment.

## VI. CONCLUSIONS

In this paper, a robust RGB stereo visual odometry method using both point and line features was proposed mainly in dynamic scenes. In order to cope with the reduction of robustness and accuracy of visual odometry systems by dynamic objects, the *dynamic grid* method that can efficiently mark dynamic regions and remove point features on dynamic objects without depth information and other sensors was proposed. In addition, to make full use of the structural information of line features, the horizontal re-projection error of the line features was introduced into the cost function to further improve the motion estimation accuracy. Finally, the proposed method had been compared with three different systems, such

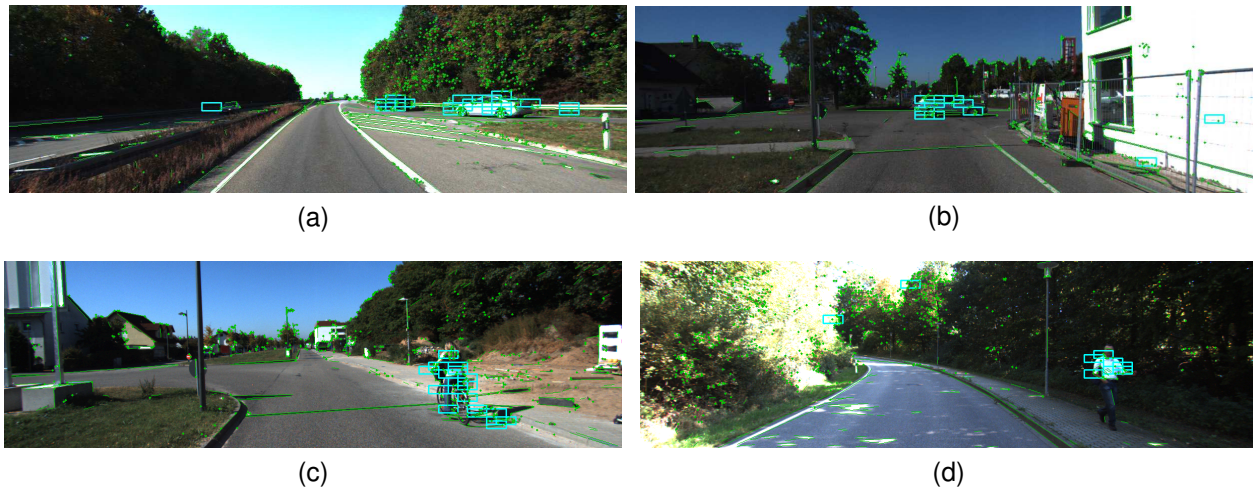


Fig. 7. Dynamic scenes on the *KITTI* dataset and the effect of dynamic grids on dynamic regions. The blue boxes represent the dynamic grids. (a) Moving cars in *KITTI-01*. (b) Moving car in *KITTI-06*. (c) The person riding a bike in *KITTI-06*. (d) The pedestrian in *KITTI-09*.

TABLE V  
MEAN ABSOLUTE AND RELATIVE RMSE ERRORS IN KITTI DATASET.

Seq.	ours w/dynamic grid		ours wo/dynamic grid	
	APE	RPE	APE	RPE
00	<b>11.221715</b>	0.040752	13.236462	<b>0.038351</b>
01	<b>182.531449</b>	<b>1.019784</b>	319.707988	1.306922
02	21.654051	0.064572	<b>10.960957</b>	<b>0.055898</b>
03	6.094158	0.032278	<b>5.946504</b>	<b>0.031802</b>
04	2.207623	0.054315	<b>2.015523</b>	<b>0.052209</b>
05	<b>4.403628</b>	0.019534	7.060361	<b>0.019145</b>
06	<b>4.428359</b>	<b>0.044869</b>	4.440736	0.056673
07	5.216922	<b>0.062928</b>	<b>4.725139</b>	0.064078
08	<b>7.443639</b>	0.043877	12.509229	<b>0.042731</b>
09	<b>4.823906</b>	<b>0.066494</b>	13.612393	0.070549
10	<b>2.282632</b>	<b>0.032286</b>	2.786268	0.033558

as `stvo_pl`, `ORB_SLAM2` front end, and `BoPLW` front end on two different datasets like *KITTI* and *EuRoC MAV*. The experimental result showed that our proposal can produce a more robust and accurate result in most scenes, especially in dynamic ones.

Future work will focus on introducing features with more geometric information, such as planes and cubes, into the system to further improve the accuracy of estimation and create a more informative map. In addition, using deep learning to improve the ability of the system to deal with dynamic scenes is also a meaningful research direction.

#### REFERENCES

- [1] T. Qin, P. Li, and S. Shen, “Vins-mono: A robust and versatile monocular visual-inertial state estimator,” *IEEE Transactions on Robotics*, vol. 34, no. 4, pp. 1004–1020, 2018.
- [2] Z. Liu, D. Shi, R. Li, W. Qin, Y. Zhang, and X. Ren, “Plc-vio: Visual-inertial odometry based on point-line constraints,” *IEEE Transactions on Automation Science and Engineering*, 2021.
- [3] Y. He, J. Zhao, Y. Guo, W. He, and K. Yuan, “Pl-vio: Tightly-coupled monocular visual-inertial odometry using point and line features,” *Sensors*, vol. 18, no. 4, p. 1159, 2018.
- [4] R. Sahdev, B. X. Chen, and J. K. Tsotsos, “Indoor localization in dynamic human environments using visual odometry and global pose refinement,” in *2018 15th Conference on Computer and Robot Vision (CRV)*, pp. 360–367, IEEE, 2018.
- [5] M. Ouyang, Z. Cao, P. Guan, Z. Li, C. Zhou, and J. Yu, “Visual-gyroscope-wheel odometry with ground plane constraint for indoor robots in dynamic environment,” *IEEE Sensors Letters*, vol. 5, no. 3, pp. 1–4, 2021.
- [6] R. Mur-Artal and J. D. Tardós, “Orb-slam2: An open-source slam system for monocular, stereo, and rgb-d cameras,” *IEEE Transactions on Robotics*, vol. 33, no. 5, pp. 1255–1262, 2017.
- [7] B. Kitt, A. Geiger, and H. Lategahn, “Visual odometry based on stereo image sequences with ransac-based outlier rejection scheme,” in *2010 IEEE Intelligent Vehicles Symposium*, pp. 486–492, IEEE, 2010.
- [8] E. Rublee, V. Rabaud, K. Konolige, and G. Bradski, “Orb: An efficient alternative to sift or surf,” in *2011 International Conference on Computer Vision*, pp. 2564–2571, Ieee, 2011.
- [9] D. G. Lowe, “Distinctive image features from scale-invariant keypoints,” *International Journal of Computer Vision*, vol. 60, no. 2, pp. 91–110, 2004.
- [10] R. G. Von Gioi, J. Jakubowicz, J.-M. Morel, and G. Randall, “Lsd: A fast line segment detector with a false detection control,” *IEEE Transactions on Pattern Analysis and Machine Intelligence*, vol. 32, no. 4, pp. 722–732, 2008.
- [11] L. Zhang and R. Koch, “An efficient and robust line segment matching approach based on lbd descriptor and pairwise geometric consistency,” *Journal of Visual Communication and Image Representation*, vol. 24, no. 7, pp. 794–805, 2013.
- [12] J. Sola, T. Vidal-Calleja, J. Civera, and J. M. M. Montiel, “Impact of landmark parametrization on monocular ekf-slam with points and lines,” *International Journal of Computer Vision*, vol. 97, no. 3, pp. 339–368, 2012.

- [13] X. Luo, Z. Tan, and Y. Ding, “Accurate line reconstruction for point and line-based stereo visual odometry,” *IEEE Access*, vol. 7, pp. 185108–185120, 2019.
- [14] A. Bartoli and P. Sturm, “Structure-from-motion using lines: Representation, triangulation, and bundle adjustment,” *Computer Vision and Image Understanding*, vol. 100, no. 3, pp. 416–441, 2005.
- [15] R. Gomez-Ojeda, F.-A. Moreno, D. Zuniga-Noël, D. Scaramuzza, and J. Gonzalez-Jimenez, “PI-slam: A stereo slam system through the combination of points and line segments,” *IEEE Transactions on Robotics*, vol. 35, no. 3, pp. 734–746, 2019.
- [16] X. Zuo, X. Xie, Y. Liu, and G. Huang, “Robust visual slam with point and line features,” in *2017 IEEE/RSJ International Conference on Intelligent Robots and Systems (IROS)*, pp. 1775–1782, IEEE, 2017.
- [17] A. Pumarola, A. Vakhitov, A. Agudo, A. Sanfeliu, and F. Moreno-Noguer, “PI-slam: Real-time monocular visual slam with points and lines,” in *2017 IEEE International Conference on Robotics and Automation*, pp. 4503–4508, IEEE, 2017.
- [18] C. Kerl, J. Sturm, and D. Cremers, “Robust odometry estimation for rgb-d cameras,” in *2013 IEEE International Conference on Robotics and Automation*, pp. 3748–3754, IEEE, 2013.
- [19] T. Whelan, H. Johannsson, M. Kaess, J. J. Leonard, and J. McDonald, “Robust real-time visual odometry for dense rgb-d mapping,” in *2013 IEEE International Conference on Robotics and Automation*, pp. 5724–5731, IEEE, 2013.
- [20] J. Engel, T. Schöps, and D. Cremers, “Lsd-slam: Large-scale direct monocular slam,” in *European Conference on Computer Vision*, pp. 834–849, Springer, 2014.
- [21] J. Engel, V. Koltun, and D. Cremers, “Direct sparse odometry,” *IEEE Transactions on Pattern Analysis and Machine Intelligence*, vol. 40, no. 3, pp. 611–625, 2017.
- [22] G. Zhang, J. H. Lee, J. Lim, and I. H. Suh, “Building a 3-d line-based map using stereo slam,” *IEEE Transactions on Robotics*, vol. 31, no. 6, pp. 1364–1377, 2015.
- [23] R. Gomez-Ojeda, J. Briales, and J. Gonzalez-Jimenez, “PI-svo: Semi-direct monocular visual odometry by combining points and line segments,” in *2016 IEEE/RSJ International Conference on Intelligent Robots and Systems*, pp. 4211–4216, IEEE, 2016.
- [24] J. H. Lee, S. Lee, G. Zhang, J. Lim, W. K. Chung, and I. H. Suh, “Outdoor place recognition in urban environments using straight lines,” in *2014 IEEE International Conference on Robotics and Automation*, pp. 5550–5557, IEEE, 2014.
- [25] C. Akinlar and C. Topal, “Edlines: A real-time line segment detector with a false detection control,” *Pattern Recognition Letters*, vol. 32, no. 13, pp. 1633–1642, 2011.
- [26] T. Koletschka, L. Puig, and K. Daniilidis, “Mevo: Multi-environment stereo visual odometry,” in *2014 IEEE/RSJ International Conference on Intelligent Robots and Systems*, pp. 4981–4988, IEEE, 2014.
- [27] R. Gomez-Ojeda and J. Gonzalez-Jimenez, “Robust stereo visual odometry through a probabilistic combination of points and line segments,” in *2016 IEEE International Conference on Robotics and Automation (ICRA)*, pp. 2521–2526, IEEE, 2016.
- [28] T. Zhu and H. Ma, “Challenges of dynamic environment for visual-inertial odometry,” in *2018 3rd International Conference on Robotics and Automation Engineering (ICRAE)*, pp. 82–86, IEEE, 2018.
- [29] H. Kim, P. Kim, and H. J. Kim, “Moving object detection for visual odometry in a dynamic environment based on occlusion accumulation,” in *2020 IEEE International Conference on Robotics and Automation*, pp. 8658–8664, IEEE, 2020.
- [30] D.-H. Kim and J.-H. Kim, “Effective background model-based rgb-d dense visual odometry in a dynamic environment,” *IEEE Transactions on Robotics*, vol. 32, no. 6, pp. 1565–1573, 2016.
- [31] Q. Sun, Y. Tang, C. Zhang, C. Zhao, F. Qian, and J. Kurths, “Unsupervised estimation of monocular depth and vo in dynamic environments via hybrid masks,” *IEEE Transactions on Neural Networks and Learning Systems*, 2021.
- [32] Y. Wan, W. Gao, S. Han, and Y. Wu, “Dynamic object-aware monocular visual odometry with local and global information aggregation,” in *2020 IEEE International Conference on Image Processing*, pp. 603–607, IEEE, 2020.
- [33] A. Geiger, P. Lenz, C. Stiller, and R. Urtasun, “Vision meets robotics: The kitti dataset,” *The International Journal of Robotics Research*, vol. 32, no. 11, pp. 1231–1237, 2013.
- [34] M. Burri, J. Nikolic, P. Gohl, T. Schneider, J. Rehder, S. Omari, M. W. Achtelik, and R. Siegwart, “The euroc micro aerial vehicle datasets,” *The International Journal of Robotics Research*, vol. 35, no. 10, pp. 1157–1163, 2016.
- [35] K. Qian, W. Zhao, K. Li, X. Ma, and H. Yu, “Visual slam with boplw pairs using egocentric stereo camera for wearable-assisted substation inspection,” *IEEE Sensors Journal*, vol. 20, no. 3, pp. 1630–1641, 2019.